metals

MDPI

Article

Characterization of Interfacial Reaction Layers Between a Zn-5Al-3Mg Solder Alloy and Cu Substrate

Jee-Hwan Bae [1], Yena Kwon [1], Seung-Moon Baek [1], Choong-Do Lee [2] and Cheol-Woong Yang [1,*]

[1] School of Advanced Materials Science and Engineering, Sungkyunkwan University, Suwon 16419, Republic of Korea
[2] Department of Materials Science and Engineering, Inha Technical College, Incheon 22212, Republic of Korea; cdlee@inhatc.ac.kr
* Correspondence: cwyang@skku.edu

Abstract

The interfacial reaction between solder and substrate is a critical factor governing joint reliability, making it essential to understand the formation and stability of interfacial reaction layers when developing new high-temperature lead-free solders. This study investigates the interfacial reaction layers formed in Zn-5Al-3Mg solder/Cu substrate joints soldered at 693 K under vacuum. With a binary Zn-Al solder, the Cu substrate is progressively consumed by Zn, and the intermediate phases $CuZn_4$, Cu_5Zn_8, and CuZn nucleate and grow concurrently at the solder interface. The addition of a minor amount of Mg to the Zn-Al alloy, however, fundamentally alters this reaction sequence. Transmission electron microscopy analyses, including scanning transmission electron microscopy–energy-dispersive X-ray spectroscopy (STEM-EDS), energy-filtered TEM (EF-TEM), and electron diffraction, reveal three distinct interfacial layers: an outer Mg_2Zn_{11} layer, a middle two-phase mixture of $CuZn_4/Mg_2CuZn_3$, and an inner Cu_5Zn_8 layer adjacent to the Cu substrate. The biphasic $CuZn_4/Mg_2CuZn_3$ mixture layer is shown to form via a quasi-peritectic reaction governed by sequential four-phase equilibria in the Zn-Mg-Cu ternary system. These findings demonstrate that minor Mg additions redirect the interfacial reaction pathway between Zn-Al-based solders and Cu substrates, providing new insight for the design of high-temperature Pb-free solder systems.

Keywords: lead-free solder; joint reliability; interface structure; analytical electron microscopy; quasi-peritectic reaction

1. Introduction

High-temperature solders are widely employed in industrial packaging applications, such as step soldering for automotive and power electronics, to produce reliable electronic devices with a high level of miniaturization and integration [1,2]. In particular, high-temperature solders used in step soldering must have a solidus temperature higher than the secondary reflow temperature (~523 K) of the Sn-based solder packaging, while their liquidus temperature must remain below the glass transition temperature (~673 K) of the polymer-based substrate materials [3].

Beyond conventional reflow soldering, several alternative bonding technologies are widely regarded as more robust solutions for high-temperature packaging. Eutectic Au-20Sn solder, with a moderate melting point of 553 K, offers excellent wettability and high joint strength and remains the incumbent choice for aerospace- and military-grade

Check for updates

Academic Editor: Zhengwei Li

Received: 11 July 2026
Revised: 5 August 2026
Accepted: 9 August 2026
Published: 12 August 2026

Copyright: © 2026 by the authors. Licensee MDPI, Basel, Switzerland. This article is an open access article distributed under the terms and conditions of the Creative Commons Attribution (CC BY) license.

power modules [4]; gold–germanium (Au-12Ge) soldering and silver-sintering die attach both achieve die shear strengths exceeding 100 MPa with essentially no degradation after thousands of thermal cycles [5]. Transient-liquid-phase (TLP) and full-intermetallic-compound (full-IMC) bonding, typically based on Cu-Sn or Ag-Sn reactions, can likewise be processed at 523–533 K yet yield joints that remain solid up to 753–873 K once the low-melting-point constituent is fully consumed, with shear strengths of 20–60 MPa reported after prolonged high-temperature aging [6,7]. These approaches, however, carry substantial cost or process penalties: Au-based solders remain expensive and are restricted to a narrow eutectic processing window [4]; sintered-Ag joints generally require an Ag- or other noble-metal-finished substrate to achieve a reliable bond, rather than the bare Cu substrate widely used in power packaging, and sintered-Cu joints are prone to oxidation during processing unless a reducing atmosphere is used [5]; and TLP/full-IMC bonding requires a lengthy, tightly controlled interdiffusion step to fully convert the low-melting-point phase, adding process complexity. Zn-Al-based solders, by contrast, can be joined directly to bare Cu substrates by conventional reflow, without precious metals, applied pressure, or protective atmospheres—making them attractive wherever process simplicity and cost outweigh the need for the largest possible operating temperature margin. Their principal drawbacks, however, are an inherently poor wettability and a susceptibility to oxidation and corrosion associated with the high chemical activity of Zn—an inherent limitation relative to Bi-Ag and other high-temperature candidates noted in the literature [6]—compounded by a melting range (643–673 K) that leaves comparatively little margin below the ~673 K glass-transition limit of polymer-based substrates noted above. These limitations are precisely what motivate the alloying strategy examined in this study.

Several candidate alloy systems have been investigated as high-temperature Pb-free solders, each with distinct advantages and limitations that ultimately favor a Zn-Al-based approach. Sn-Sb alloys [8,9] near the peritectic composition (Sn-5Sb) exhibit a melting point of only ~512 K and have been studied for their tensile creep behavior, with stress exponents ranging from about 3.5 to 9.5 depending on alloying additions and test temperature [8]; their interfacial reactions with Cu form Cu_6Sn_5 and Cu_3Sn layers that grow linearly with the square root of reaction time, indicating diffusion-controlled growth [9], and minor additions of Ag or Cu raise the ultimate tensile strength of Sn-5Sb from 32.4 MPa to as high as 40.0 MPa through the formation of Ag_3Sn and Cu-Sn intermetallic compounds [8]; nevertheless, this comparatively low melting range restricts Sn-Sb alloys to less demanding step-soldering applications. Bi-Ag alloys [3,10,11] offer a higher eutectic melting point of 535.7 K and affordable cost, and their tensile strength and ductility improve with increasing Ag content [10] and can be further enhanced by minor rare-earth doping without a substantial melting-point penalty [11]; however, Bi-Ag forms no interfacial intermetallic compound with Cu substrates, relying instead on mechanical bonding through grain-boundary grooving, and produces brittle $NiBi_3$/NiBi compounds that degrade joint strength when Ni-based metallizations are used [3]—an interfacial-bonding behavior that is inherently harder to control than intermetallic-mediated joints. Zn-Sn alloys [12–14] form well-defined Cu-Zn intermetallic layers (γ-Cu_5Zn_8 and ε-$CuZn_5$) without any Cu-Sn compound, giving joining tensile strengths of 22–32 MPa comparable to conventional Sn-37Pb/Cu joints that increase as Sn content decreases [12]; a TiN diffusion barrier can suppress this Cu-Zn intermetallic growth and thereby maintain joint strength even after 2000 thermal cycles [13], and impression creep testing of Zn-20Sn, Zn-30Sn, and Zn-40Sn solders gives stress exponents of 4.0–6.1 and activation energies of 40.0–45.3 kJ mol^{-1}, consistent with a dislocation-climb-controlled creep mechanism [14]; achieving comparable long-term reliability, however, requires this additional diffusion-barrier layer, which adds cost and process complexity.

Among these systems, Zn-Al-based alloys [15–17] remain the most practical candidate for high-temperature step soldering for the cost and process reasons described above. They offer a high thermal conductivity—about 135.7 W/K·m for a Zn-based solid solution near its eutectic melting point [16], roughly twice that of conventional Pb-5Sn solder [18]—and a correspondingly lower coefficient of thermal expansion [18], while remaining substantially less costly than Au- or Ag-based alternatives. Ternary alloying has already been used to tune the mechanical properties of Zn-Al solders: Zn-Al-Cu compositions with a melting range of 643–673 K achieve a Vickers hardness of 94–123 HV and tensile strength of 255–300 MPa, both substantially higher than Bi-2.5Ag (15 HV, 34 MPa) and Pb-5Sn (8.9 HV, 15 MPa) [15], although increasing the Al content in Zn-Cu-Al alloys promotes microstructural coarsening via the four-phase transformation $\alpha + \varepsilon \rightarrow T' + \eta$ and correspondingly lowers creep resistance [17]. In the Zn-Al-Mg system specifically, increasing Al content raises the ultimate tensile strength and fracture strain (up to 189.7 MPa and 11.3% for Zn-6Al), whereas Mg additions to Zn-5Al further increase hardness but reduce both tensile strength and elongation and raise electrical resistivity [19]. Interfacial reactions between such ternary Zn-Al-based solders and Cu substrates, as well as between binary Zn-Al alloys and Cu, consistently form the same set of binary Cu-Zn intermediate phases—$CuZn_4$, Cu_5Zn_8, and CuZn [20,21]; for example, Zn-Al-Ge alloys form these same three IMC layers at the Cu interface, with Ge lowering the alloy's melting temperature through a monotectoid reaction analogous to that of the binary Zn-Al system [21]. These precedents show that Cu, Ge, and related minor additions modify the mechanical and thermal properties of Zn-Al solders without altering the fundamental character of the Cu-Zn interfacial reaction.

The oxidation and corrosion susceptibility noted above is, in fact, a principal reason Au-based, full-IMC, and sintered alternatives are often favored over Zn-based solders in the literature [4–6]. Mg is a notable alloying addition for Zn-Al solders: additions of Mg to Zn-5Al have been shown to increase hardness, whereas they simultaneously reduce tensile strength and ductility and raise electrical resistivity [19]—a trade-off directly relevant to the long-term reliability of a solder joint. Corrosion studies of cast Zn-Al-Mg alloys indicate that the effect of Mg on corrosion resistance is similarly non-monotonic: a fine, uniformly distributed $MgZn_2$ phase at low Mg content improves corrosion resistance relative to the binary Zn-Al alloy, whereas higher Mg content coarsens the microstructure and promotes galvanic corrosion between the Zn matrix and Mg_2Zn_{11}, ultimately degrading corrosion resistance [22]. Unlike Cu or Ge, however, Mg forms its own binary intermetallic compound with Zn (Mg_2Zn_{11}) and, together with Cu diffusing from the substrate, participates in ternary invariant reactions governed by quasi-peritectic rather than simple eutectic equilibria: phase diagram studies of the Zn-Mg-Cu system have identified several such invariant reactions, capable of producing mixed-phase interfacial regions [23], and four-phase equilibrium reactions of this type are known, in general ternary systems, to yield microstructural features that cannot be predicted from binary-system behavior alone [24,25]. Consequently, the effect of Mg addition on the interfacial reaction between Zn-Al-based solders and Cu substrates cannot be inferred from the Cu- or Ge-modified precedents described above and, despite Mg's well-established bulk effects, remains uncharacterized. Because Mg addition is also known to further reduce the wettability of Zn-Al alloys, joining of Mg-containing Zn-Al solders is typically carried out under vacuum to mitigate oxidation-related wetting difficulties, an approach adopted in the present study. This vacuum-based, flux-free approach is standard practice in high-reliability applications—such as power-electronics die-attach and hermetically sealed aerospace, RF, and biomedical packages—where joint reliability depends on minimizing voids and eliminating flux residues altogether, making the Zn-Al-Mg system investigated here directly relevant despite the added process complexity.

Reliability losses in electronic systems are more often attributable to solder-joint failure than to device malfunction, and as device miniaturization progresses and bulk solder thickness decreases, the interfacial reaction layer plays an increasingly dominant role in overall joint behavior [26,27]. The interaction between Zn-Al-based solders and Cu substrates—the most common metallization in electronic assemblies—is therefore central to joint reliability [20,21]; yet, as discussed above, the effect of Mg addition on this interaction—and, in particular, the mechanism by which the resulting ternary and quasi-peritectic phases form—has not been systematically characterized. In this study, we address this gap by characterizing the interfacial reaction layers formed between a Zn-5Al-3Mg solder alloy and a Cu substrate joined at 693 K under vacuum using a combination of analytical electron microscopy techniques and by establishing the quasi-peritectic reaction pathway governing their formation.

2. Materials and Methods

2.1. Synthesis and Joining

Zn-5wt%Al-3wt%Mg (hereinafter, the unit of wt% is omitted) solder alloys were produced by alloying pure Zn (99.99%) and the Al-38Mg master alloy using a high-frequency induction furnace. Compositional homogeneity of the fabricated solder alloy was ensured by using high-purity raw materials melted in a high-frequency induction furnace; large-area scanning electron microscopy-energy-dispersive X-ray spectrometry (SEM-EDS) analyses performed at multiple locations across the solder cross-section confirmed a uniform overall composition.

Solder sheets were sliced from the resulting ingot and cut into pieces measuring 10 mm × 10 mm × 1 mm. Cu substrates (10 mm × 10 mm × 0.4 mm) were prepared from cold-rolled Cu sheets (99.96%, Nilaco, Tokyo, Japan). The Cu sheets were polished with 0.3 μm alumina powder to remove the surface oxide layer, ultrasonically cleaned, rinsed with ethanol, and dried; the solder alloy sheets were processed using the same procedure. The solder alloy and Cu substrate sheets were then stacked and placed in a quartz-tube furnace heated to 693 K, where they were joined for 10 min under vacuum without the use of flux to form the joined assemblies. Joining was performed under vacuum to mitigate the oxidation-related wetting difficulties that Mg addition is known to exacerbate in Zn-Al-based alloys.

2.2. Characterization Techniques

The melting-temperature range of the synthesized solder alloy was determined using differential scanning calorimetry (DSC; Exstar 6000, Seiko, Tokyo, Japan). X-ray diffraction (XRD; D8 Advance, Bruker Corp., Billerica, MA, USA) was performed to identify the major crystalline phases present in the as-fabricated solder alloy, where phase domains are sufficiently coarse and well-crystallized for reliable diffraction-peak identification. Because the interfacial reaction layers examined in Section 3.2 onward are sub-micron in scale, well below the effective spatial resolution of XRD-based phase mapping, their characterization instead relied primarily on STEM-based techniques. Because the scale of the microstructural features of interest was below the spatial resolution of the scanning electron microscope (SEM; JSM-7000F, JEOL Ltd., Tokyo, Japan), the microstructure and chemical composition were primarily characterized by transmission electron microscopy device (TEM; JEM-ARM200F, JEOL Ltd., Tokyo, Japan) equipped with a scanning transmission electron microscopy (STEM) attachment, an energy-dispersive X-ray spectrometer (EDS; Elite T 1071, Gatan, Inc., Pleasanton, CA, USA), and an energy-filtered TEM (EF-TEM) system (GIF 965 Quantum ER, Gatan, Inc., Pleasanton, CA, USA). Various electron diffraction techniques—including nano-beam electron diffraction (NBED), selected-area electron diffraction (SAED), and convergent-beam electron diffraction (CBED)—were additionally employed to determine the crystallographic phases formed at the joint interface [28]. Diffraction pattern indexing was confirmed by comparison with simulated patterns gen-

erated using the Java Electron Microscopy Simulation (JEMS) software package (Version 4.7231U2018b30) [29]. Cross-sectional TEM specimens were prepared using a focused ion beam instrument (FIB; JIB-4601F, JEOL Ltd., Tokyo, Japan).

3. Results and Discussion

3.1. Characterization of the Synthesized Solder Alloy

The DSC heating curve for the fabricated Zn-5Al-3Mg solder alloy is presented in Figure 1a. With reference to the phases identified from the XRD pattern in Figure 1b, the first endothermic peak, at 556.4 K, is attributed to the monotectoid reaction in which the Al-rich face-centered-cubic (fcc) phase and hexagonal-close-packed (hcp) Zn transform into a Zn-rich fcc phase; a single-phase solid solution of Al in Zn has been reported to form through this reaction [20]. The second, most prominent endothermic peak, at 616.7 K, corresponds to a eutectic melting reaction in which the Zn-rich fcc phase and hcp Zn transform into liquid phases. These two endothermic peaks are commonly observed in other Zn-Al-based solder alloys [21]. The third endothermic peak, at 621.3 K, is attributed to the transformation of the Mg_2Zn_{11} phase—identified in the XRD pattern—into a liquid phase [21].

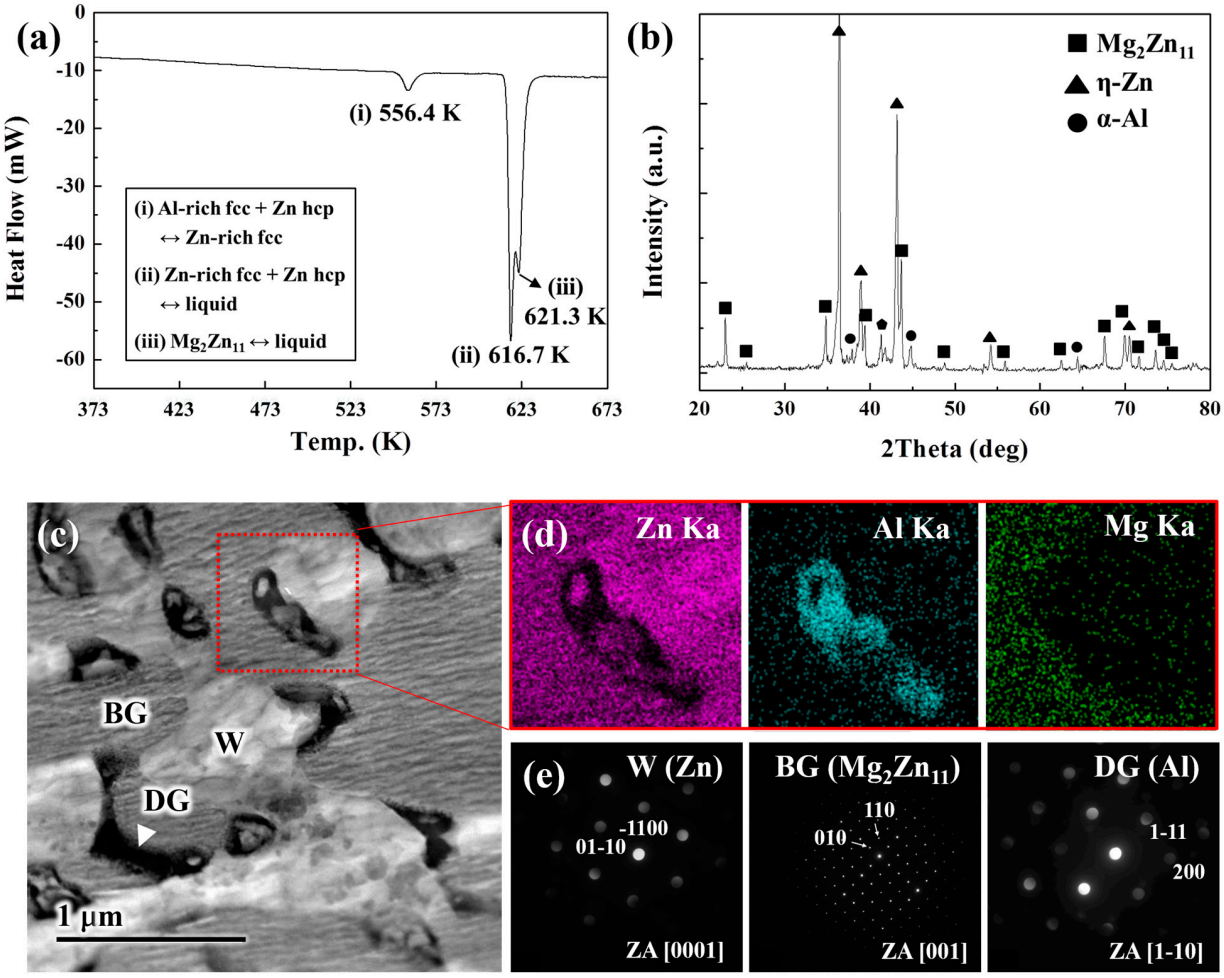
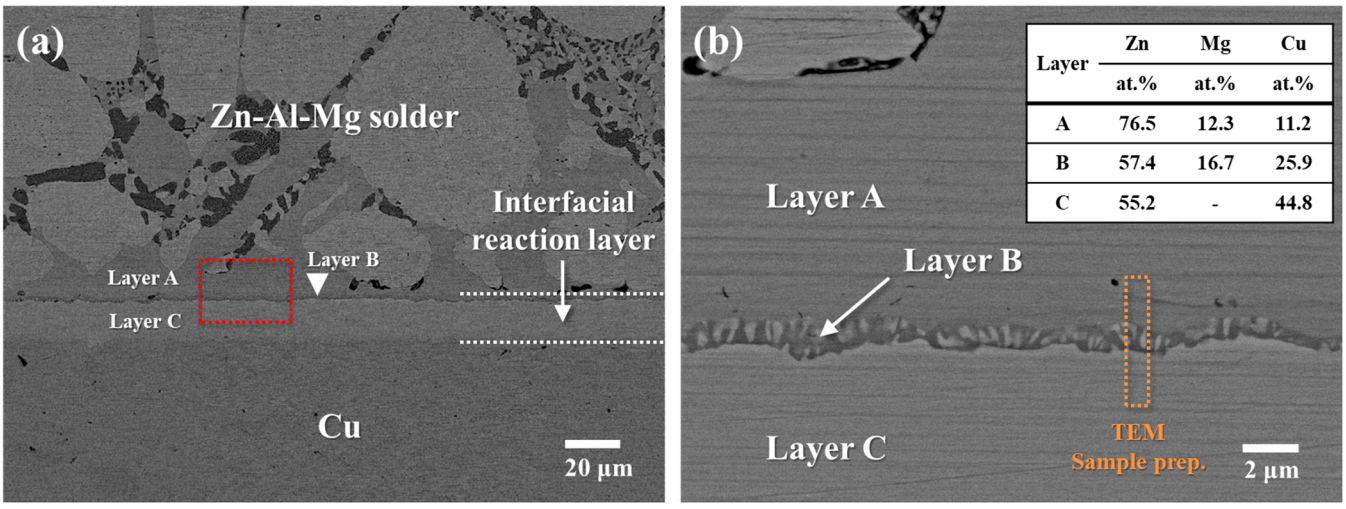


Figure 1. Analytical electron microscopy results for the fabricated Zn-5Al-3Mg solder alloy: (**a**) differential scanning calorimetry (DSC) heating curve; (**b**) X-ray diffraction (XRD) pattern; (**c**) scanning transmission electron microscopy (STEM) high-angle annular dark field (HAADF) image, where W, BG, and DG denote the "white", "bright gray", and "dark gray" regions, respectively; (**d**) STEM energy dispersive X-ray (EDS) mapping images showing the elemental distribution; and (**e**) selected-area and nano-beam electron diffraction patterns obtained from each region. Z.A. denotes the zone axis.

Figure 1c shows a STEM high-angle annular dark-field (HAADF) image, in which contrast varies with the atomic number of the constituent elements; brighter regions correspond to areas enriched in the heavier element (Zn). EDS mapping [Figure 1d] and point analyses indicate that the white ('W') region consists solely of Zn, the bright-gray ('BG') region comprises Zn and Mg, and the dark-gray ('DG') region comprises Zn and Al. Figure 1e shows SAED and NBED patterns obtained from the three regions marked 'W', 'BG', and 'DG' in Figure 1c, corresponding to their relative brightness. Combined chemical and diffraction analyses confirm that the 'W' regions correspond to the hcp Zn phase, the 'BG' regions correspond to the Mg_2Zn_{11} phase (Zn and Mg), and the 'DG' regions correspond to a Zn-substituted Al phase—consistent with the STEM-EDS results (probe size: 0.7 nm) and with the phases identified by XRD. The average composition of the 'BG' regions was determined to be ~84 at.% Zn and ~16 at.% Mg, while that of the 'DG' regions was ~11 at.% Zn and ~89 at.% Al.

3.2. Characterization of Interfacial Reaction Layers

Figure 2 shows SEM images of the Zn-5Al-3Mg/Cu interface after joining at 693 K for 10 min. The inset in Figure 2b summarizes the SEM-EDS results obtained from the intermetallic layers labeled A, B, and C. Based on their chemical compositions, layers A and B are likely a Zn-Mg-Cu ternary intermetallic and/or a mixture of binary phases, while layer C is likely a binary Zn-Cu phase. Layers B and C exhibit relatively uniform thicknesses of approximately 1 μm and 17 μm, respectively, whereas layer A shows an irregular thickness ranging from several to several tens of micrometers depending on location. Notably, these EDS results indicate that the interfacial reaction layers formed in the Zn-5Al-3Mg solder joint differ from the $CuZn_4$, Cu_5Zn_8, and CuZn layers commonly observed at the interface between binary Zn-Al-based solder alloys and Cu substrates [20,21]. This comparison is based on interfacial reaction layers reported for binary Zn-Al/Cu joints in the literature [20,21]; parallel experiments on undoped Zn-Al/Cu joints were not performed in the present study, and a direct side-by-side comparison under identical joining conditions is planned as part of follow-up work.



Layer	Zn	Mg	Cu
	at.%	at.%	at.%
A	76.5	12.3	11.2
B	57.4	16.7	25.9
C	55.2	-	44.8

Figure 2. Scanning electron microscopy (SEM) images of the Zn-5Al-3Mg/Cu interface after joining at 693 K for 10 min: (**a**) overview of the solder/Cu interface, with the red box indicating the region enlarged in (**b**); (**b**) magnified view of the interfacial reaction layer within the boxed region in (**a**), with the region from which the cross-sectional TEM specimen was subsequently extracted marked by the orange dashed box.

TEM was employed to analyze the interfacial microstructure in greater detail. Figure 3 presents TEM imaging, EDS analysis, and diffraction results for the Zn-5Al-3Mg/Cu interface after joining at 693 K for 10 min, and Table 1 lists the corresponding quantitative STEM-EDS results for interfacial reaction layers A, B, and C. As shown in Figure 3a and Table 1, three distinct layers—differentiated by image contrast and elemental composition—were observed, consistent with the SEM-EDS results. Layer A consisted of Mg, Zn, and Cu, whereas layer C comprised only Zn and Cu; SAED was used to identify the phases present in both layers.

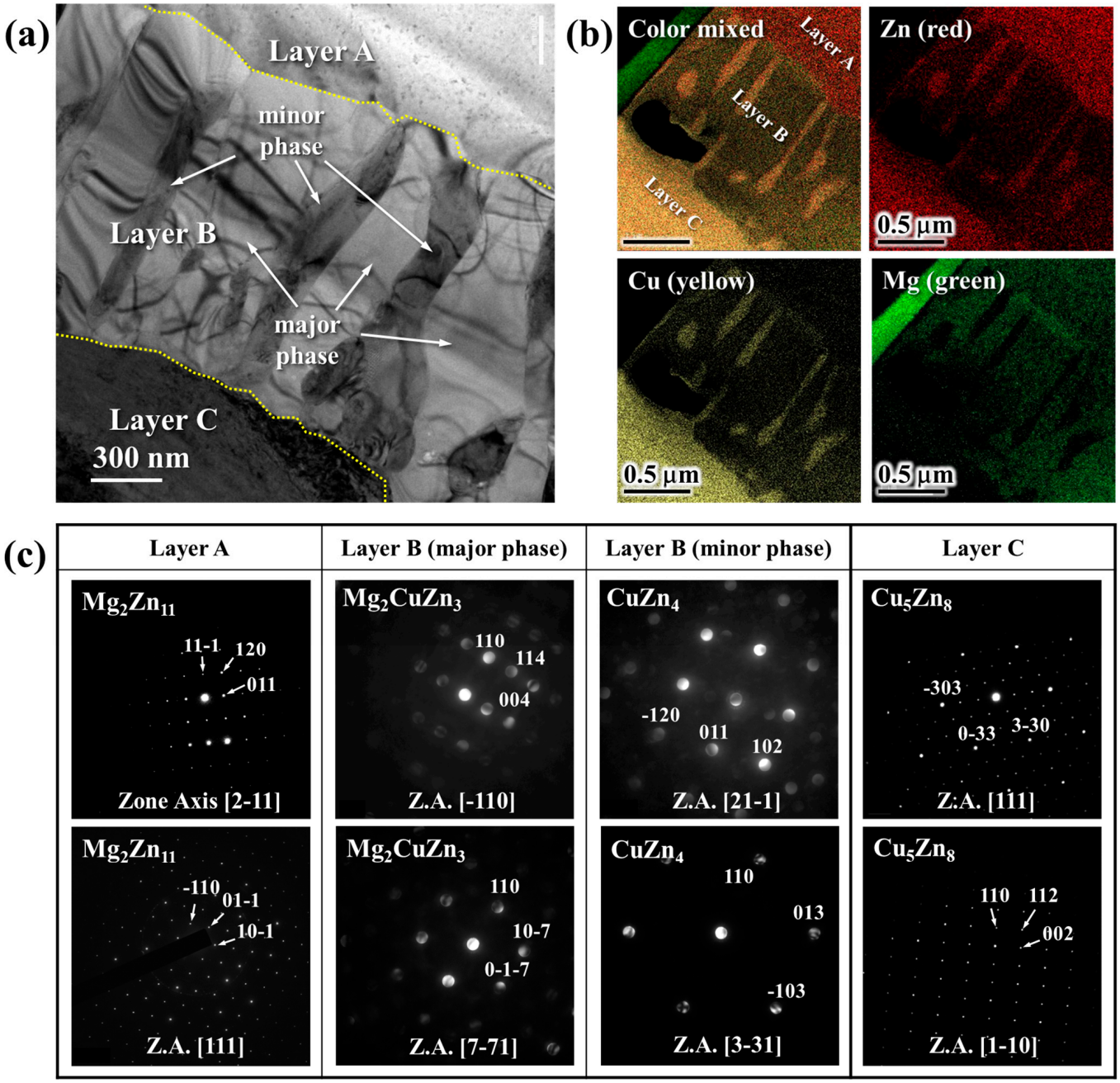


Figure 3. (**a**) Transmission electron microscopy (TEM) micrograph of a Zn-5Al-3Mg/Cu interface; (**b**) energy-filtered TEM (EF-TEM) elemental mapping images for Zn (red), Cu (yellow), and Mg (green); and (**c**) selected-area and nano-beam electron diffraction patterns of the interfacial reaction layers A, B, and C shown in (**a**) labeled with the identified phases and zone axes.

Table 1. Elemental compositions of the interfacial reaction layers, as determined by scanning transmission electron microscopy-energy dispersive X-ray spectroscopy (STEM-EDS) analysis.

Layer	Composition (at.%)			Expected Phase
	Zn	Mg	Cu	
A	73.02	13.87	13.10	$Mg_2(Zn,Cu)_{11}$
B (minor phase)	68.66	-	31.34	$CuZn_4$
B (major phase)	44.71	34.69	20.60	Mg_2CuZn_3
C	57.02	-	42.98	Cu_5Zn_8

According to Table 1, layer A has a composition of ~73 at.% Zn, ~14 at.% Mg, and ~13 at.% Cu, consistent with a Mg_2Zn_{11} phase into which Cu diffused during joining, forming $Mg_2(Zn,Cu)_{11}$. Layer C has an average composition of ~57 at.% Zn and ~43 at.% Cu, consistent with Cu_5Zn_8, the most common intermetallic compound in the Cu-Zn system. Both phase assignments were confirmed by indexing of the SAED patterns obtained from each layer [Figure 3c]. The SAED patterns of layer A were indexed as two distinct zone-axis patterns, $[21\bar{2}]$ and [111], of the Mg_2Zn_{11} phase (cubic, space group $Pm\bar{3}$, a = 0.8552 nm), while those of layer C were indexed as the [111] and $[1\bar{1}0]$ zone axis patterns of the Cu_5Zn_8 phase (cubic, space group $I\bar{4}3m$, a = 0.8878 nm).

Layer B, located between layers A and C, exhibited two phases—a major and a minor phase—distinguishable by their area fraction and contrast in the STEM-HAADF image [Figure 3a]. Figure 3b shows the corresponding EF-TEM elemental mapping series (Zn, Cu, and Mg) for the region in Figure 3a, in which composition changes sharply across the interphase boundaries. Notably, the bright region in the upper-left corner of the Mg (green) EF-TEM map corresponds to the protective Pt layer deposited during FIB specimen preparation; Pt signals were detected during Mg analysis because the Pt $O_{2,3}$ edge (52 eV) lies close in energy to the Mg $L_{2,3}$ edge (51 eV). The minor phase of layer B had an average composition of 68.66 at.% Zn and 31.34 at.% Cu, consistent with a $CuZn_4$ phase (hexagonal, space group $P6_3/mmc$, a = 0.2742 nm, c = 0.4294 nm, $\gamma = 120°$); this assignment was confirmed by NBED patterns acquired along two distinct zone axes, $[21\bar{1}]$ and $[3\bar{3}1]$ [Figure 3c].

The major phase of layer B was identified as a ternary phase based on STEM-EDS point analysis (Table 1) and mapping [Figure 3b]. Its Mg and Cu contents (~34.69 at.% Mg and ~20.60 at.% Cu) were higher than those of layer A (~13.87 at.% Mg and ~13.10 at.% Cu), while its Zn content (~44.71 at.% Zn) was lower than that of layer A (~73.02 at.% Zn). This phase was identified as Mg_2CuZn_3 (hexagonal, space group $P6_3/mmc$, a = 0.5124 nm, c = 1.682 nm, $\gamma = 120°$) by combined diffraction pattern indexing and chemical analysis [Figure 3c]. Possible compositions for this phase were assessed with reference to the Zn-Mg-Cu ternary phase diagram [23]. An invariant equilibrium reaction, $L + \gamma \leftrightarrow \varepsilon + \tau$, occurring at a composition of 12 at.% Cu, 9.9 at.% Mg, and 78.1 at.% Zn has been reported [23], where γ, ε, and τ correspond to the Cu_5Zn_8, $CuZn_4$, and Mg_2CuZn_3 solid phases, respectively.

Two techniques—primitive unit cell volume measurement and JEMS simulation—were used to confirm the phases present in layer B, because several Cu-Zn intermetallic phases (e.g., CuZn, Cu_5Zn_8, $CuZn_4$) can exhibit similar diffraction characteristics and closely related lattice parameters, making phase discrimination from a single technique alone difficult.

First, convergent-beam electron diffraction (CBED) analysis was carried out to identify the phase within a small sampled area using the primitive-unit-cell-volume method [30]. Because the primitive unit cell volume is a characteristic material constant, the phase of interest can be readily identified by comparing the primitive cell volume of an unknown phase—calculated from its CBED pattern—with the known values of reference phases. In

a CBED pattern, the internal angle (ANG) between the transmitted beam disk (D1) and the diffracted beam disk (D2), together with the high-order Laue zone (HOLZ) ring radius (CRAD), can be directly measured; the primitive unit cell volume (V) of the unknown phase is then calculated from these measured values using the following relation [28,30]:

$$V = (CL^2 \times \lambda^3)/[D_1 \times D_2 \times \sin(ANG) \times (1 - \cos(\tan^{-1}(CRAD/CL)))] \quad (1)$$

where CL is the camera length, calibrated using a Si standard at 200 keV, and λ is the wavelength of the incident electron beam.

Figure 4 shows CBED patterns obtained from areas comprising the major and minor phases of layer B; the corresponding measured constants and calculated primitive cell volumes are listed in Table 2. The volumes calculated from the CBED patterns in Figure 4a and b are 0.381 nm^3 and 0.029 nm^3, respectively, closely matching the theoretical volumes of Mg_2CuZn_3 and $CuZn_4$. The theoretical volume of Mg_2CuZn_3 ($P6_3/mmc$, $V = 0.5124^2 \times 1.682 \times \sin(120°)$) is 0.382 nm^3, and that of $CuZn_4$ ($P6_3/mmc$, $V = 0.2742^2 \times 0.4294 \times \sin(120°)$) is 0.028 nm^3.

Table 2. Measured constants and calculated primitive unit cell volumes obtained from the convergent-beam electron diffraction (CBED) patterns of layer B shown in Figure 4a,b.

Pattern	CL (mm)	D_1 (mm)	D_2 (mm)	CRAD (mm)	ANG (deg.)	λ (nm)	Primitive Unit Cell Volume (nm^3)
(a)	89.0	10.6	8.8	26.3	64.3	0.00251	0.381
(b)	89.0	16.5	19.2	46.5	90	0.00251	0.029

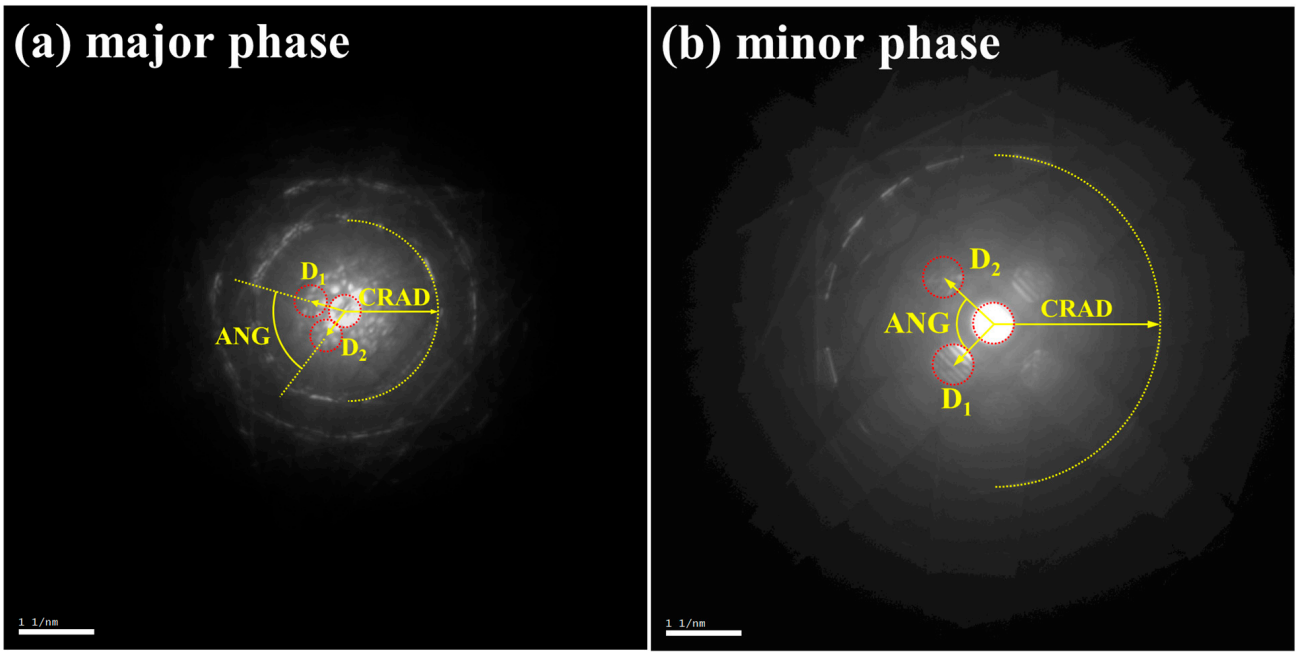


Figure 4. Convergent-beam electron diffraction (CBED) patterns acquired from the (**a**) major and (**b**) minor phases of layer B.

Second, SAED and CBED patterns for the mixed phases in layer B were simulated using the Java-based crystallography software JEMS (Version 4.3905). Crystal information files for the Mg_2CuZn_3 and $CuZn_4$ phases were constructed from literature data obtained from a public crystallographic database and previously reported studies [15,23]. As shown in Figure 5, the experimentally acquired SAED and CBED patterns for layer B closely

matched the corresponding patterns simulated by JEMS for the same zone axes. Together, these results confirm that layer B consists of a mixture of Mg_2CuZn_3 (major phase) and $CuZn_4$ (minor phase).

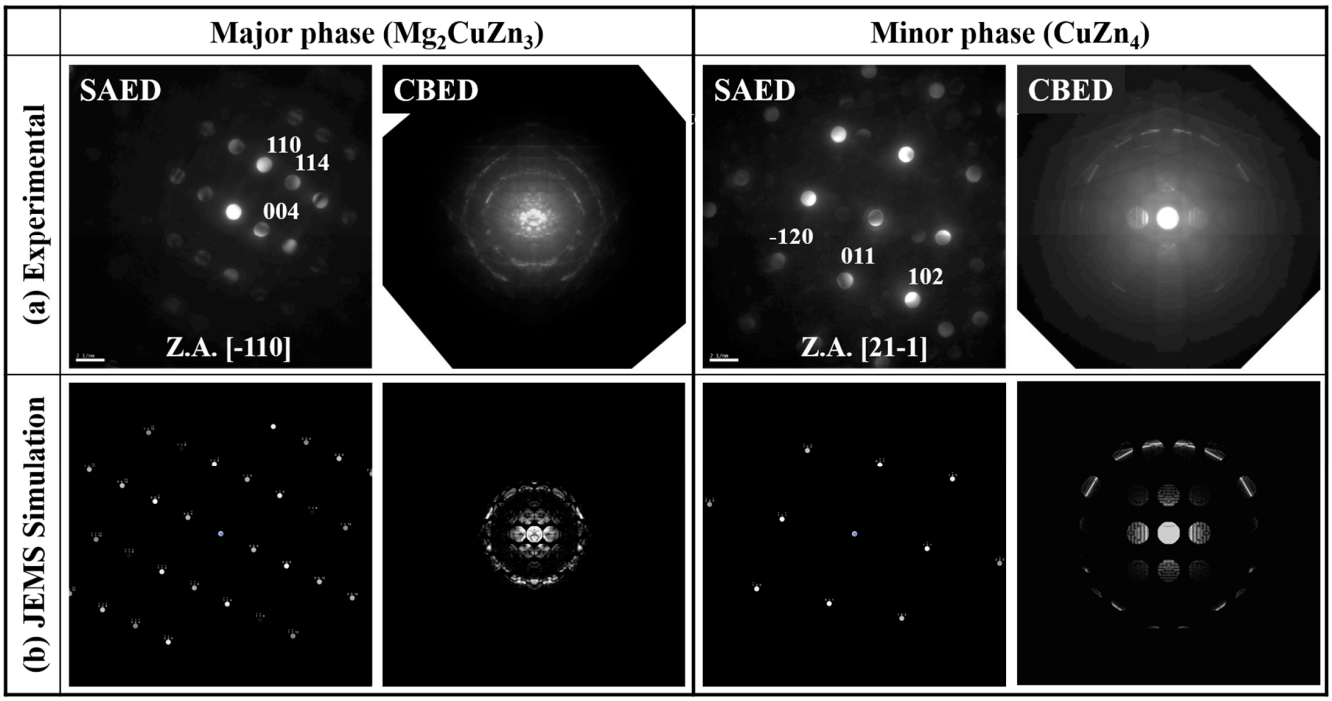


Figure 5. (**a**) Experimentally acquired selected-area electron diffraction (SAED) and convergent-beam electron diffraction (CBED) patterns of layer B, and (**b**) corresponding patterns simulated using the Java Electron Microscopy Simulation (JEMS) software for the same zone axes.

Finally, the interfacial reaction layers identified here differ from those recently reported for the same Zn-5Al-3Mg/Cu system joined under different conditions [31], which we attribute to the substantially different joining conditions employed in that study (ultrasound-assisted soldering at a lower temperature for a much shorter time) versus the furnace joining at 693 K for 10 min used here. Ongoing work in our group is examining the effects of Mg content, joining temperature, and joining time on the resulting interfacial reaction layers, with preliminary results indicating that the mixed layer identified here forms only under specific processing conditions.

3.3. Formation Mechanism of the Two-Phase Mixed Layer

The formation of the two-phase structure in layer B can be explained by a four-phase equilibrium reaction characteristic of ternary systems, as described by Prince [24] and Rhines [25]. This equilibrium corresponds to a quasi-peritectic phase transformation:

$$L + \alpha \leftrightarrow \beta + \gamma \quad (2)$$

where L denotes a liquid phase, and α, β, and γ denote distinct solid phases. As noted by Prince [24], the four-phase quasi-peritectic equilibrium is preceded, at higher temperatures, by two three-phase equilibria—each either peritectic or eutectic in character. As temperature decreases, these three-phase equilibria (L-α-β and L-α-γ) converge at the quasi-peritectic plane to form the four-phase equilibrium L-α-β-γ. Below this temperature, the reaction products give rise to two new three-phase equilibria, α-β-γ and L-β-γ, which descend in temperature from the quasi-peritectic isotherm.

Figure 6, constructed from the thermodynamic dataset of Liang et al. [23] and simplified to highlight only the reaction path relevant to the present study (see [32] for the complete liquidus projection with all phase field boundaries), shows the solidification path of the stacked Zn-Al-Mg solder and Cu substrate assembly during joining. During heat treatment, the Cu substrate is consumed by Zn, and γ-Cu_5Zn_8 forms simultaneously at the solder/substrate interface. As the temperature decreases, the primary γ-Cu_5Zn_8 continues to grow, and the composition of the liquid—enriched by diffused Cu—evolves toward the quasi-peritectic reaction point U_4 (78.1 at.% Zn, 9.9 at.% Mg, 12.0 at.% Cu), corresponding to the following reaction:

$$L + \gamma\text{-}Cu_5Zn_8 \leftrightarrow \varepsilon\text{-}CuZn_4 + \tau\text{-}Mg_2CuZn_3 \ (785\ K). \quad (3)$$

At point U_4, the τ-Mg_2CuZn_3 (major) and ε-$CuZn_4$ (minor) phases begin to crystallize, consuming the γ-Cu_5Zn_8 phase. The experimental joining temperature (693 K) is lower than the theoretical temperature of U_4 predicted from the phase diagram (785 K), because in the present system solidification occurs through the reaction of the molten Zn-Mg binary alloy with the Cu substrate, rather than within a pre-formed molten Zn-Mg-Cu ternary alloy.

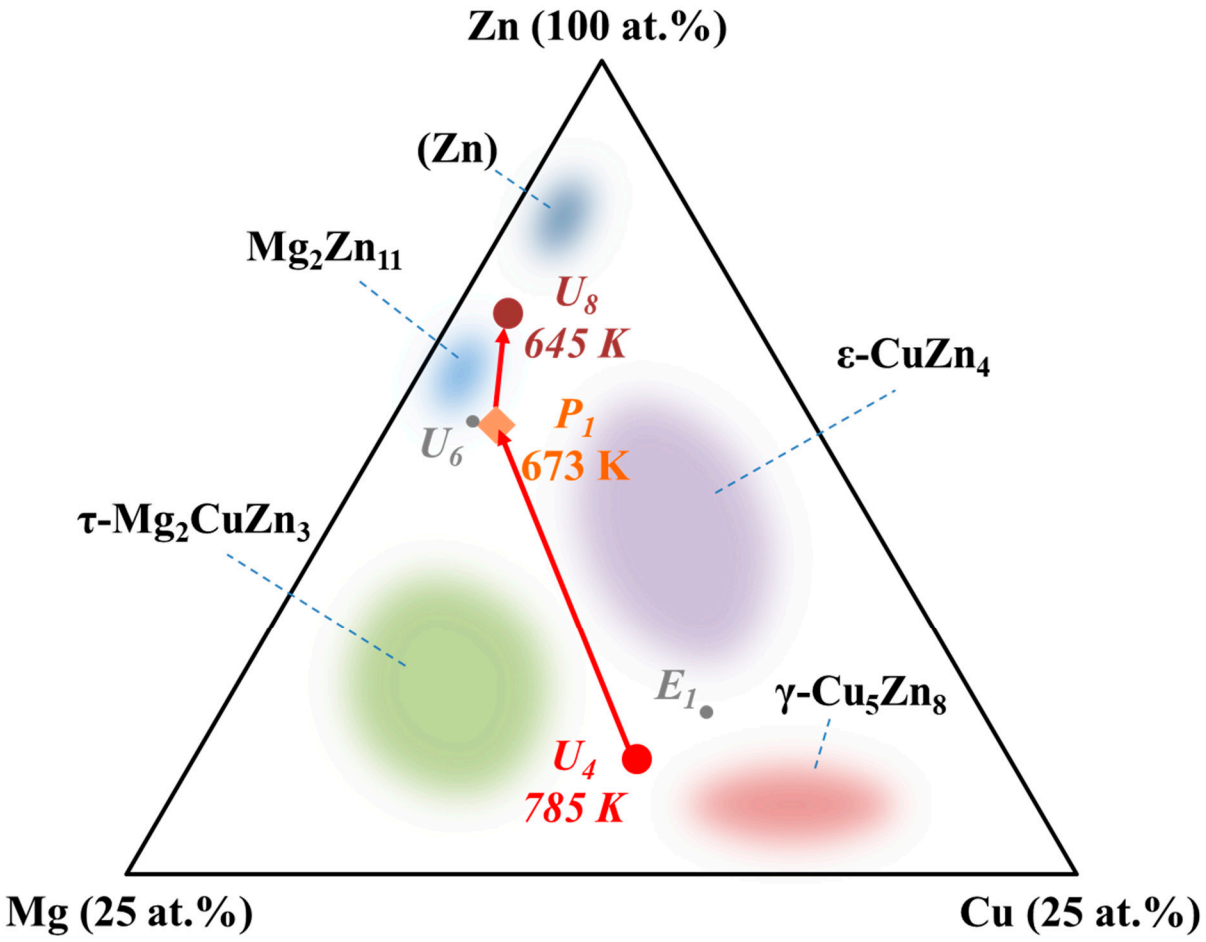


Figure 6. Schematic reaction path through the Zn-rich corner of the Cu-Mg-Zn ternary liquidus surface; not to scale. The path traces the evolution of the residual liquid composition through the quasi-peritectic reaction at U_4 (78.1 at.% Zn, 9.9 at.% Mg, 12.0 at.% Cu; 785 K), the ternary peritectic reaction at P_1 (88.8 at.% Zn, 8.5 at.% Mg, 2.7 at.% Cu; 673 K), and the eutectic reaction at U_8 (92.2 at.% Zn, 6.4 at.% Mg, 1.4 at.% Cu; 645 K), corresponding to reactions (3)–(6) in the text. The nearby invariant reactions E_1 and U_6 are shown for context but are not part of the reaction sequence discussed here. Shaded regions indicate the approximate, qualitative locations of the (Zn), ε-$CuZn_4$, τ-Mg_2CuZn_3, Mg_2Zn_{11}, and γ-Cu_5Zn_8 phase fields and do not represent actual phase boundaries.

As the τ-Mg_2CuZn_3 and ε-$CuZn_4$ phases crystallize, the liquid composition moves along the U_4-P_1 reaction line, driven by the progressive depletion of Mg and diffused Cu in the liquid, toward the ternary peritectic point P_1, corresponding to the following reaction:

$$L + \varepsilon\text{-}CuZn_4 + \tau\text{-}Mg_2CuZn_3 \leftrightarrow Mg_2(Zn,Cu)_{11}\ (673\ K). \quad (4)$$

The formation of $Mg_2(Zn,Cu)_{11}$ in layer A results from this peritectic transformation, with Cu substitution in the Mg_2Zn_{11} structure facilitated by the similar ionic radii and crystal structure compatibility. Partial substitution of Zn by Cu in the Al-Zn-Cu-Mg system is well established [33]. At point P_1, the $Mg_2(Zn,Cu)_{11}$ phase begins to crystallize and continues to form along the P_1-U_8 reaction line, corresponding to the reaction

$$L + \varepsilon\text{-}CuZn_4 \leftrightarrow Mg_2(Zn,Cu)_{11} + (Zn)\ (645–673\ K), \quad (5)$$

until the liquid composition reaches point U_8. Finally, along the U_8-e_7 reaction line, corresponding to

$$L \leftrightarrow Mg_2Zn_{11} + Zn, \quad (6)$$

the Mg_2Zn_{11} and Zn-based phases form until the liquid is fully consumed.

This complex reaction sequence explains the unique three-layer interfacial structure observed in the Mg-modified Zn-Al solder system, demonstrating how minor alloying additions can fundamentally alter interfacial reaction mechanisms and resulting microstructures.

It is noted that the $Mg_2(Zn,Cu)_{11}$ phase identified in layer A (Table 1) does not appear as a separately labeled invariant phase in the liquidus projection [23] (see [32] for the complete phase field boundaries), because it is not a distinct equilibrium phase but rather a Cu-substituted solid solution based on the Mg_2Zn_{11} phase field near the Zn-rich corner: Cu diffusing from the substrate partially substitutes for Zn within the Mg_2Zn_{11} structure during solidification (Equations (4) and (5)), while the underlying equilibrium phase relationships remain governed by the Mg_2Zn_{11} field established for the Cu-Mg-Zn system [23,32].

Figure 7 presents a schematic summary of the sequential formation of the interfacial reaction layers, illustrating the progression from the initial γ-Cu_5Zn_8 layer to the final three-layer structure (Mg_2Zn_{11}/($CuZn_4$ + Mg_2CuZn_3)/Cu_5Zn_8) via the quasi-peritectic reactions described above.

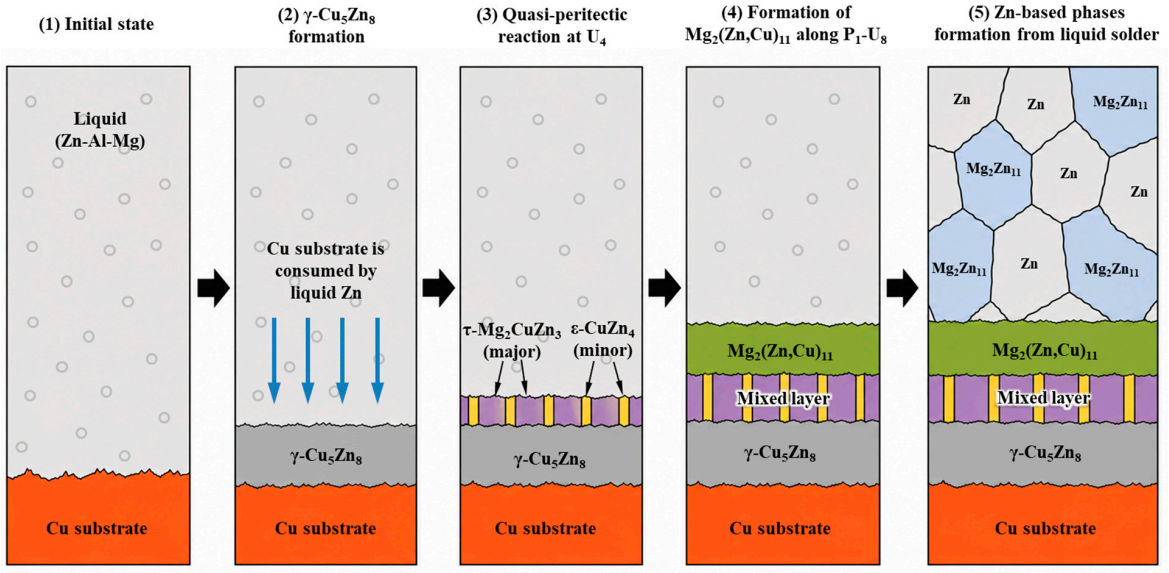


Figure 7. Schematic illustration of the sequential formation of the interfacial reaction layers in the Zn-5Al-3Mg/Cu joint, corresponding to the reaction pathway shown in Figure 6.

4. Conclusions

This study demonstrates that a minor Mg addition (3 wt%) to a Zn-5Al solder fundamentally redirects the interfacial reaction pathway with Cu substrates. Instead of the $CuZn_4$, Cu_5Zn_8, and CuZn layers typical of binary Zn-Al/Cu joints, three new interfacial reaction layers form: an outer Mg_2Zn_{11} layer, a middle biphasic mixture of $CuZn_4$ and Mg_2CuZn_3, and an inner Cu_5Zn_8 layer adjacent to the Cu substrate. Using a combination of quantitative STEM-EDS, SAED/NBED/CBED diffraction, unit-cell-volume measurement, and JEMS simulation, we show that the biphasic mixture layer forms via a quasi-peritectic reaction governed by sequential four-phase equilibria in the Zn-Mg-Cu ternary system.

These results establish a mechanistic link between minor alloying additions and interfacial phase selection: the relative thickness and continuity of the biphasic $CuZn_4/Mg_2CuZn_3$ layer can potentially be controlled through the Mg content of the solder and the joining temperature/time, since these parameters determine how closely the interfacial liquid composition approaches the U_4 and P_1 invariant points identified in this work. This provides a compositional and thermal-processing basis for tailoring interfacial microstructure in future solder and process design.

The present findings are based on a single joining condition (693 K, 10 min) and microstructural/crystallographic characterization; future work will (i) measure interfacial layer thickness over a range of joining times and temperatures to determine growth exponents, parabolic growth constants, and activation energies governing layer growth and (ii) evaluate the mechanical properties of joints containing these newly identified layers, including microhardness and shear strength, to establish the relationship between interfacial microstructure and mechanical reliability. Together, these directions will further support the application of Zn-Al-Mg solders in high-temperature, Pb-free step-soldering technologies.

Author Contributions: Conceptualization, J.-H.B. and C.-W.Y.; Methodology, J.-H.B. and C.-D.L.; Validation, J.-H.B. and C.-D.L.; Formal analysis, J.-H.B. and Y.K.; Investigation, J.-H.B., Y.K. and S.-M.B.; Resources, C.-D.L.; Data curation, J.-H.B., Y.K. and S.-M.B.; Writing—original draft, J.-H.B.; Writing—review & editing, J.-H.B., C.-D.L. and C.-W.Y.; Visualization, J.-H.B., Y.K. and S.-M.B.; Supervision, C.-W.Y.; Project administration, C.-W.Y.; Funding acquisition, C.-W.Y. All authors have read and agreed to the published version of the manuscript.

Funding: This work was supported in part by the National Research Foundation of Korea (NRF) grant funded by the Korean government (MSIP) [Grant No. 2011-0017257] and in part by the Korea Basic Science Institute (National Research Facilities and Equipment Center) grant funded by the Ministry of Education [Grant No. RS-2024-00436224].

Data Availability Statement: The original contributions presented in this study are included in the article. Further inquiries can be directed to the corresponding author.

Acknowledgments: The authors also gratefully acknowledge the support of the Cooperative Center for Research Facilities (CCRF) at Sungkyunkwan University, Korea.

Conflicts of Interest: The authors declare no conflict of interest.

References

1. Suganuma, K.; Kim, S.J.; Kim, K.S. High-temperature lead-free solders: Properties and possibilities. *JOM* **2009**, *61*, 64–71. [CrossRef]
2. Chidambaram, V.; Hattel, J.; Hald, J. Design of lead-free candidate alloys for high-temperature soldering based on the Au-Sn system. *Mater. Des.* **2010**, *31*, 4638–4645. [CrossRef]
3. Song, J.-M.; Chuang, H.-Y.; Wu, Z.-M. Interfacial reactions between Bi-Ag high-temperature solders and metallic substrates. *J. Electron. Mater.* **2006**, *35*, 1041–1049. [CrossRef]

4. Xu, J.; Wu, M.; Pu, J.; Xue, S. Novel Au-based solder alloys: A potential answer for electrical packaging problem. *Adv. Mater. Sci. Eng.* **2020**, *2020*, 4969647. [CrossRef]
5. Sabbah, W.; Azzopardi, S.; Buttay, C.; Meuret, R.; Woirgard, E. Study of die attach technologies for high temperature power electronics: Silver sintering and gold-germanium alloy. *Microelectron. Reliab.* **2013**, *53*, 1617–1621. [CrossRef]
6. Hang, C.; He, J.; Zhang, Z.; Chen, H.; Li, M. Low temperature bonding by infiltrating Sn3.5Ag solder into porous Ag sheet for high temperature die attachment in power device packaging. *Sci. Rep.* **2018**, *8*, 17111. [CrossRef] [PubMed]
7. Zhang, H.; Xu, H.; Wang, T.; Wang, S. Preparation and performance of semiconductor device bonding joints based on Cu@Sn@Ag preform. *RSC Adv.* **2023**, *13*, 35683–35688. [CrossRef] [PubMed]
8. El-Daly, A.A.; Fawzy, A.; Mohamad, A.Z.; El-Taher, A.M. Microstructural evolution and tensile properties of Sn–5Sb solder alloy containing small amount of Ag and Cu. *J. Alloys Compd.* **2011**, *509*, 4574–4582. [CrossRef]
9. Chen, S.-W.; Zi, A.-R.; Chen, P.-Y.; Wu, H.-J.; Chen, Y.-K.; Wang, C.-H. Interfacial reactions in the Sn–Sb/Ag and Sn–Sb/Cu couples. *Mater. Chem. Phys.* **2008**, *111*, 17–19. [CrossRef]
10. Song, J.-M.; Chuang, H.-Y.; Wen, T.-X. Thermal and tensile properties of Bi-Ag alloys. *Metall. Mater. Trans. A* **2007**, *38*, 1371–1375. [CrossRef]
11. Shi, Y.; Fang, W.; Xia, Z.; Lei, Y.; Guo, F.; Li, X. Investigation of rare earth-doped BiAg high-temperature solders. *J. Mater. Sci. Mater. Electron.* **2010**, *21*, 875–881. [CrossRef]
12. Lee, J.-E.; Kim, K.-S.; Suganuma, K.; Takenaka, J.; Hagio, K. Interfacial properties of Zn–Sn alloys as high temperature lead-free solder on Cu substrate. *Mater. Trans.* **2005**, *46*, 2413–2418. [CrossRef]
13. Kim, S.; Kim, K.-S.; Kim, S.-S.; Suganuma, K.; Izuta, G. Improving the reliability of Si die attachment with Zn-Sn-based high-temperature Pb-free solder using a TiN diffusion barrier. *J. Electron. Mater.* **2009**, *38*, 2668–2675. [CrossRef]
14. Mahmudi, R.; Eslami, M. Impression creep behavior of Zn-Sn high-temperature lead-free solders. *J. Electron. Mater.* **2010**, *39*, 2495–2502. [CrossRef]
15. Kim, S.-J.; Kim, K.-S.; Kim, S.-S.; Kang, C.-Y.; Suganuma, K. Characteristics of Zn-Al-Cu alloys for high temperature solder application. *Mater. Trans.* **2008**, *49*, 1531–1536. [CrossRef]
16. Aksöz, S.; Ocak, Y.; Maraşlı, N.; Keşlioğlu, K. Determination of thermal conductivity and interfacial energy of solid Zn solution in the Zn–Al–Bi eutectic system. *Exp. Therm. Fluid Sci.* **2011**, *35*, 395–404. [CrossRef]
17. Alibabaie, S.; Mahmudi, R. Microstructure and creep characteristics of Zn–3Cu–xAl ultra high-temperature lead-free solders. *Mater. Des.* **2012**, *39*, 397–403. [CrossRef]
18. Shimizu, T.; Ishikawa, H.; Ohnuma, I.; Ishida, K. Zn-Al-Mg-Ga alloys as Pb-free solder for die-attaching use. *J. Electron. Mater.* **1999**, *28*, 1172–1175. [CrossRef]
19. Rafid, S.; Soshi, S.S.; Ahmed, A.F.; Gafur, M.A. Effect of Al on Zn and Mg on Zn-Al as Pb-free solder alloy. *Mater. Sci. Appl.* **2025**, *16*, 252–268.
20. Takaku, Y.; Felicia, L.; Ohnuma, I.; Kainuma, R.; Ishida, K. Interfacial reaction between Cu substrates and Zn-Al base high-temperature Pb-free solders. *J. Electron. Mater.* **2008**, *37*, 314–323. [CrossRef]
21. Haque, A.; Won, Y.S.; Haseeb, A.S.M.A.; Masjuki, H.H. Investigations on Zn-Al-Ge alloys as high temperature die attach material. In Proceedings of the 3rd Electronics System Integration Technology Conference (ESTC), Berlin, Germany, 13–16 September 2010; pp. 1–5.
22. Hammam, R.E.; Abdel-Gawad, S.A.; Moussa, M.E.; Shoeib, M.; El-Hadad, S. Study of microstructure and corrosion behavior of cast Zn-Al-Mg alloys. *Int. Met.* **2023**, *17*, 2794–2807. [CrossRef]
23. Liang, P.; Seifert, H.J.; Lukas, H.L.; Ghosh, G.; Effenberg, G.; Aldinger, F. Thermodynamic modelling of the Cu-Mg-Zn ternary system. *Calphad* **1998**, *22*, 527–544. [CrossRef]
24. Prince, A. *Alloy Phase Equilibria*; Elsevier: Amsterdam, The Netherlands, 1966.
25. Rhines, F.N. *Phase Diagrams in Metallurgy: Their Development and Application*; McGraw-Hill: New York, NY, USA, 1956.
26. Huang, Z.; Conway, P.P.; Jung, E.; Thomson, R.C.; Liu, C.; Loeher, T.; Minkus, M. Reliability issues in Pb-free solder joint miniaturization. *J. Electron. Mater.* **2006**, *35*, 1761–1772. [CrossRef]
27. Zeng, K.; Tu, K.N. Six cases of reliability study of Pb-free solder joints in electronic packaging technology. *Mater. Sci. Eng. R* **2002**, *38*, 55–105. [CrossRef]
28. Le Page, Y.; Downham, D.A. Determination of the primitive unit cell volume from convergent-beam electron diffraction patterns. *J. Electron Microsc. Tech.* **1991**, *18*, 437–439. [CrossRef] [PubMed]
29. Stadelmann, P.A. EMS-a software package for electron diffraction analysis and HREM image simulation in materials science. *Ultramicroscopy* **1987**, *21*, 131–145. [CrossRef]
30. Kim, G.-H.; Ahn, J.-P. Phase identification of nano-phase materials using convergent beam electron diffraction (CBED) technique. *Korean J. Electron Microsc.* **2006**, *36*, 47–56.
31. Kolenak, R.; Kostolny, I.; Drapala, J.; Zackova, P.; Kuruc, M. Direct ultrasonic soldering of AlN ceramics with copper substrate using Zn-Al-Mg solder. *Metals* **2020**, *10*, 160. [CrossRef]

32. Lukas, H.L.; Rogl, P.; Ghosh, G.; Effenberg, G. Cu-Mg-Zn. In *Light Metal Systems, Landolt-Börnstein New Series IV/11A4*; Springer: Berlin/Heidelberg, Germany, 2006; pp. 252–265.
33. Becker, H.; Dopita, M.; Stráska, J.; Málek, P.; Vilémová, M.; Rafaja, D. Microstructure and properties of spark plasma sintered Al-Zn-Mg-Cu alloy. *Acta Phys. Pol. A* **2015**, *128*, 602–605. [CrossRef]

Disclaimer/Publisher's Note: The statements, opinions and data contained in all publications are solely those of the individual author(s) and contributor(s) and not of MDPI and/or the editor(s). MDPI and/or the editor(s) disclaim responsibility for any injury to people or property resulting from any ideas, methods, instructions or products referred to in the content.